

Thermally Driven Interfacial Degradation between $\text{Li}_7\text{La}_3\text{Zr}_2\text{O}_{12}$ Electrolyte and $\text{LiNi}_{0.6}\text{Mn}_{0.2}\text{Co}_{0.2}\text{O}_2$ Cathode

Younggyu Kim, Dongha Kim, Roland Bliem, Gülin Vardar, Iradwikanari Waluyo, Adrian Hunt, Joshua T. Wright, John P. Katsoudas, and Bilge Yildiz*



Cite This: <https://dx.doi.org/10.1021/acs.chemmater.0c02261>



Read Online

ACCESS |



Metrics & More

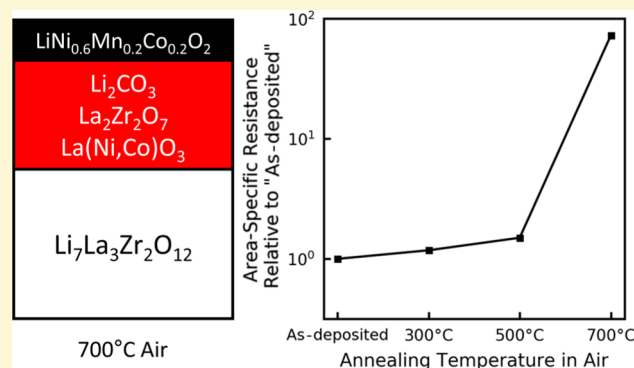


Article Recommendations



Supporting Information

ABSTRACT: Solid-state batteries offer higher energy density and enhanced safety compared to the present lithium-ion batteries using liquid electrolytes. A challenge to implement them is the high resistances, especially at the solid electrolyte interface with the cathode. Sintering at elevated temperature is needed in order to get good contact between the ceramic solid electrolyte and oxide cathodes and thus to reduce contact resistances. Many solid electrolyte and cathode materials react to form secondary phases. It is necessary to find out which phases arise as a result of interface sintering and evaluate their effect on electrochemical properties. In this work, we assessed the interfacial reactions between $\text{LiNi}_{0.6}\text{Mn}_{0.2}\text{Co}_{0.2}\text{O}_2$ (NMC622) and $\text{Li}_7\text{La}_3\text{Zr}_2\text{O}_{12}$ (LLZO) as a function of temperature in air. We prepared model systems by depositing thin-film NMC622 cathode layers on LLZO pellets. The thin-film cathode approach enabled us to use interface-sensitive techniques such as X-ray absorption spectroscopy in the near-edge as well as the extended regimes and identify the onset of detrimental reactions. We found that the Ni and Co chemical environments change already at moderate temperatures, on-setting from 500 °C and becoming especially prominent at 700 °C. By analyzing spectroscopy results along with X-ray diffraction, we identified Li_2CO_3 , $\text{La}_2\text{Zr}_2\text{O}_7$, and $\text{La}(\text{Ni},\text{Co})\text{O}_3$ as the secondary phases that formed at 700 °C. The interfacial resistance for Li transfer, measured by electrochemical impedance spectroscopy, increases significantly upon the onset and evolution of the detected interface chemistry. Our findings suggest that limiting the bonding temperature and avoiding CO_2 in the sintering environment can help to remedy the interfacial degradation.



1. INTRODUCTION

Current lithium-ion batteries using liquid electrolytes are inherently unstable because of low flash points of carbonate species.¹ Substituting the liquid electrolyte with a solid electrolyte may solve this problem and obtain high-capacity, high-power cells without flammability issues.^{2,3} Among the possible choices for the solid electrolyte, $\text{Li}_7\text{La}_3\text{Zr}_2\text{O}_{12}$ (LLZO) is a promising material system because of its relatively high conductivity, which reaches up to 10^{-1} to 1 mS/cm.⁴ In addition, its large electrochemical window permits the usage of both a high-voltage cathode and the Li metal anode.⁵ Exploiting Li metal anode could lead to the development of batteries with much higher capacity than the current lithium-ion batteries using graphite as an anode.⁶ Even with solid electrolytes such as LLZO, Li dendrites can grow through grain boundaries.^{7,8} However, there are many promising recent developments to overcome this problem.^{9–11} In addition, there has been much progress on the Li wettability on LLZO by removing the Li_2CO_3 layer, and this has already lead to significantly lowered interfacial resistance at the LLZO|Li interface.¹²

In contrast, progress at the cathode|LLZO interface remains relatively slow. Computational studies based on first-principles and thermodynamic calculations have predicted that the interface of layered oxide cathodes with the LLZO interface is more stable compared to other interfaces that comprise sulfide electrolytes ($\text{Li}_{10}\text{GeP}_2\text{S}_{12}$ and Li_3PS_4) or other types of cathodes (LiMn_2O_4 and LiFePO_4).^{13,14} However, the actual demonstration of all solid batteries using layered oxide cathode and LLZO has been dissatisfactory so far. For example, cells comprising LiCoO_2 (LCO) and LLZO sintered at 700 °C suffered from poor capacity (35 mAh/g).¹⁵ The main issue here arises from the secondary-phase formation at the cathode|LLZO interface during heat treatment, which leads to high interfacial resistance. Even though there have been attempts to

Received: May 29, 2020

Revised: October 5, 2020

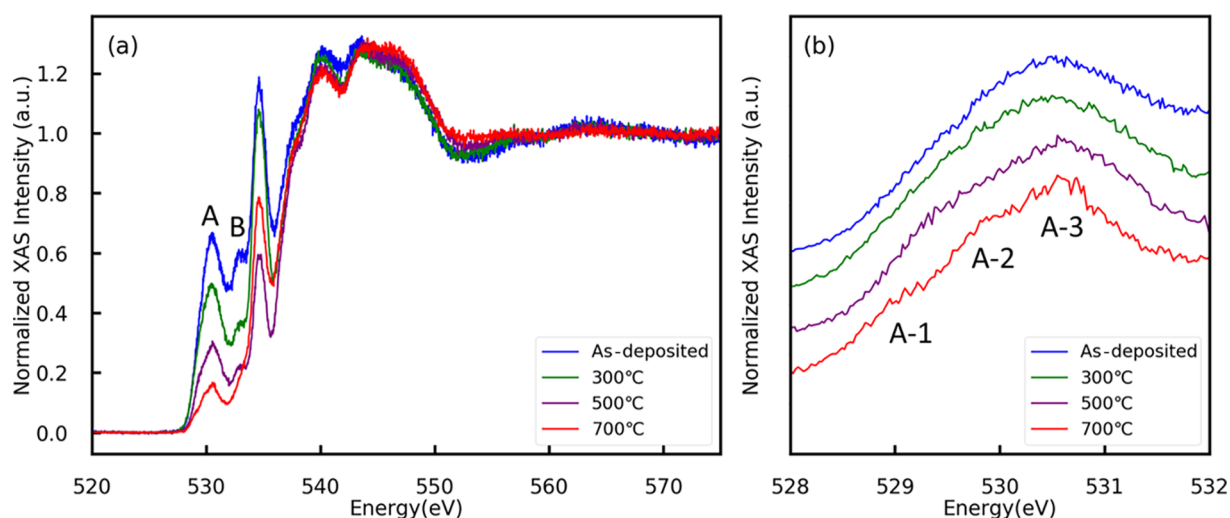


Figure 1. (a) O K-edge X-ray absorption spectra (partial fluorescence yield mode) for 100 nm NMC622/LLZO in the as-deposited state and annealed at different temperatures in air for 4 h. (b) Region A normalized by highest point in each region. Data shifted by arbitrarily chosen offset for comparison.

characterize chemical reactions between layered oxide cathodes and LLZO, a consensus on the nature of the decomposition products is missing,^{16–18} and the onset conditions for the degradation remain unexplored. Furthermore, theoretical studies have predicted the formation of Li-rich phases such as Li_2NiO_3 , Li_5CoO_4 , and Li_2MnO_3 ,^{13,19} but they have not predicted phases that could form between the LLZO and the layered oxide cathode. This prediction does not match well with experimental findings in the literature^{15–17,20} as well as in our recent²¹ and present work. We believe that the discrepancy comes from the role of different chemical species and elevated temperatures in the environment, which were not considered in those calculations, and as discussed later in this paper.

Probing the cathode–solid electrolyte interface is a major challenge. X-ray diffraction (XRD) on mixed powders is a practical approach to identify reaction phases between solid electrolyte and cathode materials. However, for detecting the secondary phases with good sensitivity using this bulk approach, the reaction has to proceed significantly within the detection limit of powder XRD. Thus, it misses the ability to detect the onset conditions and identify the effect of very thin reaction zones on the charge-transfer kinetics. We have recently addressed this challenge by using thin-film cathode layers as model systems deposited on solid electrolyte pellets.²¹ This approach positions the interfacial region within the detection depth of techniques such as X-ray absorption spectroscopy (XAS). This enabled us to capture the initiation of the degradation process at relatively low temperatures and to precisely characterize the secondary phases and the reacted zone depth (on the order of nanometer scale) at the LiCoO_2 /LLZO interface.²¹

In this research, we have adopted the same thin-film cathode approach as in our recent work²¹ and have focused on the layered oxide cathode, $\text{LiNi}_{0.6}\text{Mn}_{0.2}\text{Co}_{0.2}\text{O}_2$ (NMC622) on the LLZO electrolyte. By substituting Co with Ni, it is possible to extract more electrons from the cathode during charging without triggering oxygen evolution.²² In addition, Mn incorporation gives additional stability by suppressing Ni^{4+} formation.²³ Using NMC622 could lead to cells with high

operating voltage and capacity,²⁴ and this makes the system more interesting for industrial applications.

Our approach combines synchrotron techniques [X-ray absorption near-edge spectroscopy (XANES) and extended X-ray absorption fine structure (EXAFS)] and lab-based techniques [XRD and electrochemical impedance spectroscopy (EIS)]. XRD enables preliminary phase analysis, but XRD alone is not sufficient to resolve the onset of the degradation where phases have low crystallinity and overlapping peaks. We used XANES and EXAFS to characterize the local chemical and atomic coordination environment, even at relatively low temperatures, where the onset of reactions has taken place but the products have not formed long-range order yet. By combining the results obtained from our work and former literature on the instability of layered oxides, we explain the degradation behavior at the NMC622/LLZO interface. Results showed that cation intermixing and oxidation starts at 300 °C, and the effect becomes more severe as temperature rises in air. We found formation and crystallization of Li_2CO_3 starting from 500 °C. At 700 °C, $\text{La}(\text{Ni},\text{Co})\text{O}_3$ and $\text{La}_2\text{Zr}_2\text{O}_7$ were also detected. We assessed the impact of the chemically degraded interface on the charge-transfer properties by performing EIS on symmetric NMC622/LLZO/NMC622 samples. Interfacial resistance increased with annealing temperature, showing that chemical degradation at the interface leads to blockage of Li-ion transfer through the interface.

2. EXPERIMENT DESIGN AND METHODS

In order to understand interfacial degradation between NMC622 cathode and LLZO, it is necessary to keep the interfacial region within the detection depth of characterization techniques. In our experiment, XANES experiment using soft X-rays set the upper limit of the thickness of NMC622 thin films that could be used. The thickness was chosen considering the mean free path of photons with 1 keV energy,²⁵ which is 100 nm. Samples were prepared by depositing NMC622 on top of preprepared LLZO pellets by RF sputtering at nominally room temperature conditions. After deposition, the samples were annealed at 300, 500, and 700 °C in air for 4 h. Annealing was done in air in order to consider the possible effect of CO_2 during chemical reaction. Temperature range was chosen to include the range for crystallizing layered oxide cathode thin films after deposition, which spans between 400 and 700 °C.^{26–29}

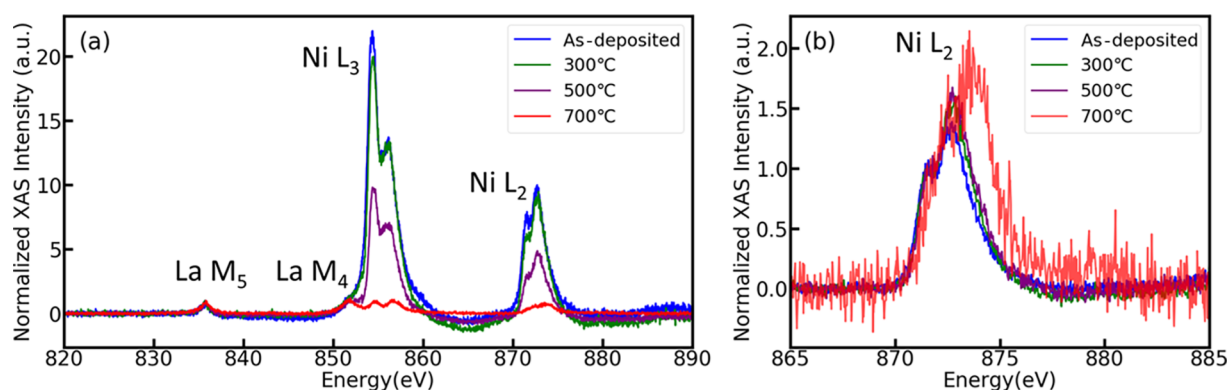


Figure 2. (a) La M_5 , La M_4 , Ni L_3 , and Ni L_2 X-ray absorption spectra (partial fluorescence yield mode) for 100 nm NMC622/LLZO in the as-deposited state and annealed at different temperatures in air. Amplitude of peaks normalized by a La M_5 peak. (b) Ni L_2 X-ray absorption spectra (partial fluorescence yield mode) for 100 nm NMC622/LLZO in the as-deposited state and annealed at different temperatures in air. Amplitude of peaks normalized by the low-energy shoulder peak.

Chemical and structural characterization was done by XANES, EXAFS, and XRD. We used samples with the same geometry for all the characterization techniques. These characterization techniques complemented each other and together led to a reliable identification of secondary phases and degradation behavior. XANES and EXAFS give information regarding oxidation state and local chemical and coordination environment of each element. By combining data obtained from those two techniques, and from XRD, we conclude which secondary phases have formed.

The effect of secondary-phase formation on charge transfer at the interface was studied by EIS. We used symmetric cells with NMC622 on both sides of the LLZO pellets. This approach let us study the effect of the cathode/electrolyte interface only, without a Li/electrolyte interface, and has simplified the analysis. NMC622 thin-film layers (60 nm thick) were deposited on both sides of LLZO by RF sputtering. Annealing conditions were the same with the samples that we used for chemical characterization. After heat treatment, the 60 nm thick Au layers were deposited on both sides as a current collector.

Experimental method details are provided in the [Supporting Information](#).

3. RESULTS

3.1. Oxidation State Obtained by XAS. The oxidation state and coordination of each element depends on the crystal in which the element resides in. Therefore, depending on the crystal structure of reactants and products, the XANES spectra present different features before and after the NMC622/LLZO interface reaction. By analyzing the spectra, we narrowed down the possible set of candidates for the formed secondary phases. We studied the near-edge regions of O K-edge, Ni L-edge, La M-edge, Co L-edge, Ni K-edge, and Co K-edge.

Figure 1 shows the O K-edge spectra for the 100 nm NMC622/LLZO samples, which were annealed at different temperatures. Feature A (528–532 eV) comes from the electronic transition stemming from hybridization of 3d orbitals of transition metals and 2p orbital of oxygen.^{30,31} According to former studies on LLZO and Li_2CO_3 including our former work, the change of shape and magnitude of this feature are solely dependent on the chemical environment change of transition metals (Ni, Co, and Mn), while O K-edge spectra from LLZO and Li_2CO_3 do not have any features in this energy range.^{20,21,32} As seen in **Figure 1a**, the magnitude of feature A gradually decreased as annealing temperature increased. This implies loss of transition metal atoms from the detection depth of XAS. This could arise from either diffusion of transition metals through NMC622/LLZO into

LLZO and out of the detection depth or a reaction and phase change involving these elements.

Interestingly, the shape of feature A changed when the sample was annealed at 700 °C, as shown in **Figure 1b**, where the intensity is normalized by the magnitude of feature A. The sample annealed at 700 °C shows a low-energy shoulder at 529 eV (A-1). This feature has not been reported by other XAS studies on NMC, even when NMC was electrochemically cycled.^{33,34} Because this feature appears after exposure to elevated temperature, we believe that it is a consequence of a major change in the chemical environment of the transition metals. The meaning of the feature will be further discussed after we present the changes in the Ni and Co $L_{2,3}$ -edges.

The loss of interfacial area can be characterized by examining the O K-edge XAS features. Feature B (532–533.5 eV) in **Figure 1** originates from bulk LLZO.²¹ Because feature B is clearly seen from the as-deposited sample, the detection depth of the O K-edge XAS includes all of the NMC622 film and the upper portion of the LLZO pellet. Lack of feature B from the sample annealed at 700 °C indicates that there is no LLZO left within the same detection depth. LLZO near the NMC interface had been completely transformed to secondary phases. Considering the geometry of the sample, the formed secondary phases completely covered the NMC622/LLZO interface.

Figure 2a shows the La M_5 edge, La M_4 edge, Ni L_3 edge, and Ni L_2 edge for each sample. We normalized data by the magnitude of La M_5 edge to compare the data. The M_4 and M_5 edges are evident from the as-deposited sample. We attributed the changes in the shape and magnitude of these peaks to interfacial reactions. By comparing the magnitude of the La and Ni edges, we can see a decrease of Ni/La elemental ratio within the detection regime as annealing temperature increased. This implies Ni diffusion into LLZO away from the XAS detection depth, similar to the behavior deduced from **Figure 1**. In addition, **Figure 2b** indicates that Ni gets more oxidized as the annealing temperature increased. In the figure, data for Ni L_2 edge were normalized with the magnitude of low-energy portion of the edge for comparison. Spectral weight shift to higher energy is explained by oxidation of Ni.^{34–36} These findings together suggest formation of secondary phases including Ni and La at 700 °C. Further justification will be given by the following data.

The Co L₃ edge shifted toward higher energy, consistent with an increase in the Co oxidation state, as the annealing temperature increased, as shown in Figure 3. Interestingly, the

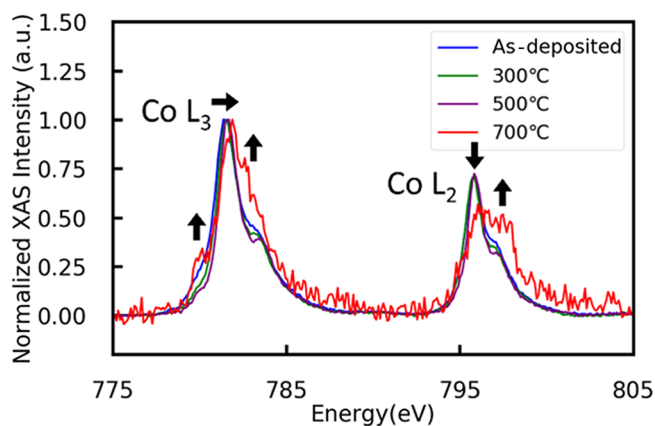


Figure 3. Co L₃, Co L₂ X-ray absorption spectra (partial fluorescence yield mode) for 100 nm NMC622/LLZO in the as-deposited state and annealed at different temperatures in air. Amplitude of peaks normalized by the Co L₃ edge.

shape of the Co L₃ edge and Co L₂ edge changed drastically at 700 °C. An increase of the pre-edge feature for the Co L₃ edge at 780 eV and spectral weight shift to higher energy for the Co L₂ edge is evident. Merz et al. reported these features from their study on doped LaCoO₃ perovskites.³⁷ The authors compared the Co L-edge shape for LaCoO₃, La_{0.7}Ce_{0.3}CoO₃, and La_{0.7}Sr_{0.3}CoO₃ and found these features (the same as our Co L_{2,3}-edge spectrum at 700 °C) for Co⁴⁺ (high spin, HS) in La_{0.7}Sr_{0.3}CoO₃. Notably, undoped LaCoO₃ did not show features for Co⁴⁺ (HS) in their study.

In our previous work on the LiCoO₂/LLZO interface, LaCoO₃ was a reaction product upon annealing.²¹ Therefore, it is reasonable to assume the formation of similar perovskite phases at the NMC622/LLZO system, as we substituted elements of the cathode layer without changing the crystal

structure. However, formation of pure LaCoO₃ cannot explain the features in Co L edge shown in Figure 3. For this reason, we propose that the secondary phase formed at 700 °C is a doped LaCoO₃. Considering the evidence of Ni/La intermixing found from Figure 2, we suggest that Ni is the likely dopant in the LaCoO₃ formed here. Introducing Ni into LaCoO₃ as a B-site dopant increases the Co⁴⁺ (HS) content, as reported by Huang.³⁸ The Co L-edge shape change shown in Huang's data matches well with the work of Merz et al. mentioned above,³⁷ and with Figure 3 shown in this work. Therefore, we can conclude that the Co oxidation state increases and becomes +4 (HS) after annealing the interface at 700 °C.

Oxidization of Ni above +2 at 700 °C, shown in Figure 2b, requires that Ni concentration in La(Ni,Co)O₃ is higher than Co. If we denote the concentration of Ni as x in LaNi _{x} Co_{1- x} O₃ ($0.5 \leq x \leq 1$), we can rewrite the charge neutrality formula as (La³⁺)(Ni²⁺)_{1- x} (Ni³⁺)_{2 x -1}(Co⁴⁺)_{1- x} (O²⁻)₃ according to Pérez's model.³⁹ In this formula, the average oxidation state of Ni is $4 - 1/x$, and it increases from +2 to +3 as the Ni concentration increases from 0.5 to 1 in La(Ni,Co)O₃. Pérez's model also states that the oxidation state of Ni is fixed to +2 for LaNi _{x} Co_{1- x} O₃ with $x \leq 0.5$. Therefore, an increase of the oxidation state of Ni above +2 (as seen from Ni L₂ edge in Figure 2b) means $x > 0.5$ in LaNi _{x} Co_{1- x} O₃. Assuming that the reaction front is at the buried interface between the LLZO and NMC, this argument is consistent with the Ni migration out of NMC622 (as seen from the decrease of Ni L₂/La M₅ ratio at 700 °C in Figure 2a), presumably occurring during La(Ni,Co)-O₃ formation.

Going back to Figure 1, oxidation of Co upon heat treatment is seen further by analyzing the O K edge carefully. Feature A-1 shown in Figure 1b is seen in materials in which Co is octahedrally coordinated by an oxygen ligand with holes.^{40,41} Miyoshi and Yamaguchi⁴⁰ found that feature A-1 became larger for La_{0.6}Sr_{0.4}CoO_{3- δ} as the oxygen partial pressure of the environment increased. In addition, Karvonen et al. showed that feature A-1 became larger as the oxygen concentration increased in SrCoO_{3- δ} .⁴¹ Oxygen concentration

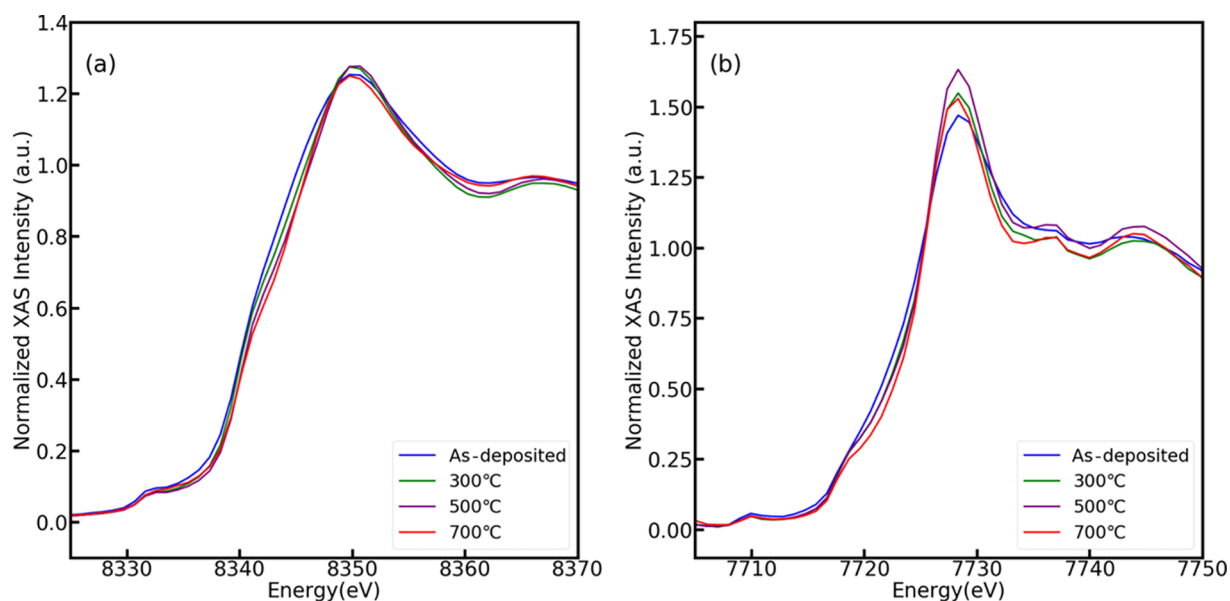


Figure 4. Ni K-edge and (b) Co K-edge X-ray absorption spectra (fluorescence yield mode) for 100 nm NMC622/LLZO in the as-deposited state and annealed at different temperatures in air.

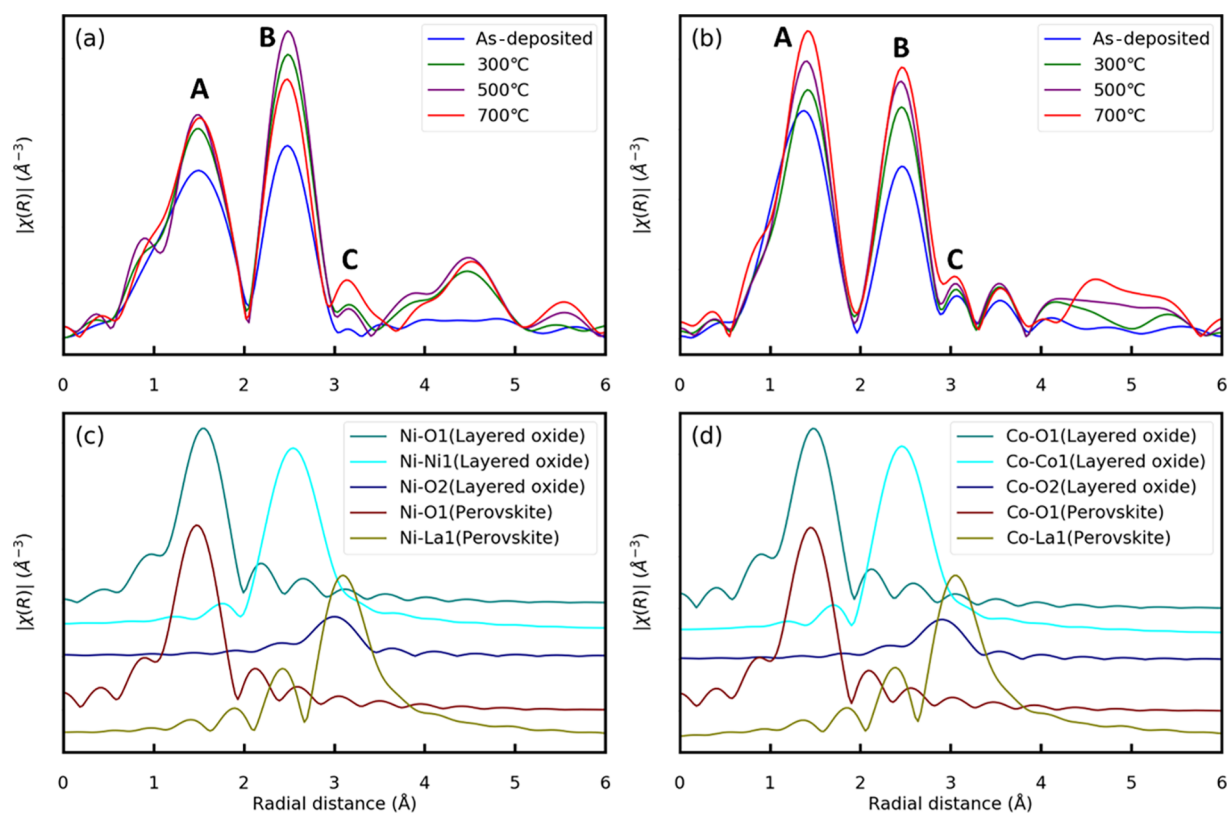


Figure 5. (a) Ni K-edge and (b) Co K-edge EXAFS data in real space. (c) Single scattering paths for LiNiO_2 (mp-25592) and LaNiO_3 (mp-1075921). (d) Single scattering paths for LiCoO_2 (mp-24850) and LaCoO_3 (mp-1068396). (Numbers after mp indicate the identity for each crystal structure in the Materials Project Database⁴⁷).

increase leads to oxidation of transition metal in those systems. Therefore, these works give further proof to the A-1 feature, indicating further oxidation of Co.

The near-edge regions of the Ni K-edge and Co K-edge spectra, shown in Figure 4, provide further support for the oxidation of Ni and Co. Data were obtained in the fluorescence yield mode. We defined the edge by taking the energy at which the normalized absorption value was 0.5.⁴² Both edges shift to higher energy as the annealing temperature increased, showing further oxidation of both Ni and Co.

Figure S1 shows the Mn L-edge spectra for the as-deposited sample and for samples annealed at 300, 500, and 700 °C. All data showed features for Mn^{4+} but did not show features corresponding to Mn with other oxidation states (Mn^{2+} and Mn^{3+}).⁴³ Therefore, the oxidation state of Mn remained the same before and after heat treatment.

3.1.1. Local Chemical Environment Change of Elements Due to Secondary-Phase Formation. Above we have deduced evidence for migration of Ni and Co out of NMC622 and formation of $\text{La}(\text{Ni},\text{Co})\text{O}_3$. Thus, we expect changes in the atomic coordination of these elements and examine the Ni K-edge and Co K-edge EXAFS. Figure 5a,b shows the Ni K-edge and Co K-edge EXAFS in *R*-space. Figure 5c,d shows ideal scattering paths for Ni and Co in layered oxides (LiNiO_2 and LiCoO_2) and in perovskites (LaNiO_3 and LaCoO_3). The scattering paths are plotted for the first, second, and third shells for layered oxides and the first and second shells for perovskites.

As can be seen in Figure 5c,d, LaNiO_3 and LaCoO_3 show almost identical scattering paths around Ni and Co, respectively. This originates from the same crystal symmetry.

Therefore, scattering paths obtained for Ni in LaNiO_3 and Co in LaCoO_3 could be used to model scattering path in $\text{La}(\text{Ni},\text{Co})\text{O}_3$. The same logic justifies using LiNiO_2 and LiCoO_2 to model the scattering path in NMC 622.

The magnitudes of feature A and feature B increase up to 500 °C for both Ni K edge and Co K edge. This shows crystallization of the sputtered NMC films because features A and B are related to the first shell and second shell of layered oxide structure, respectively.^{44–46} This crystallization trend was also reported by our former study on annealing of LiCoO_2 thin-film/LLZO system.²¹ However, the Ni K-edge EXAFS deviated from this trend at 700 °C. The magnitude of feature B dropped in comparison to the sample annealed at 500 °C, while the magnitude of feature A remained almost the same. Moreover, the magnitude of feature C increased compared to other temperature conditions.

Simultaneous increase of feature C and decrease of feature B at 700 °C can be explained by formation of the $\text{La}(\text{Ni},\text{Co})\text{O}_3$ phase. Figure 5a,c shows that the scattering paths from the second shell of NMC622 mainly contributes to feature B of the Ni K-edge EXAFS. Therefore, Ni migrating out of NMC622 to form the perovskite phase leads to the decrease of feature B. Moreover, we can see that the second shell of $\text{La}(\text{Ni},\text{Co})\text{O}_3$ has a major contribution to feature C. Therefore, formation of the perovskite phase increases the feature C intensity. We also note that the first shells of both $\text{La}(\text{Ni},\text{Co})\text{O}_3$ and NMC622 contribute to feature A. Therefore, decomposition of NMC622 and formation of $\text{La}(\text{Ni},\text{Co})\text{O}_3$ would not change feature A, consistent with the lack of any change in feature A of the Ni K edge in Figure 5a.

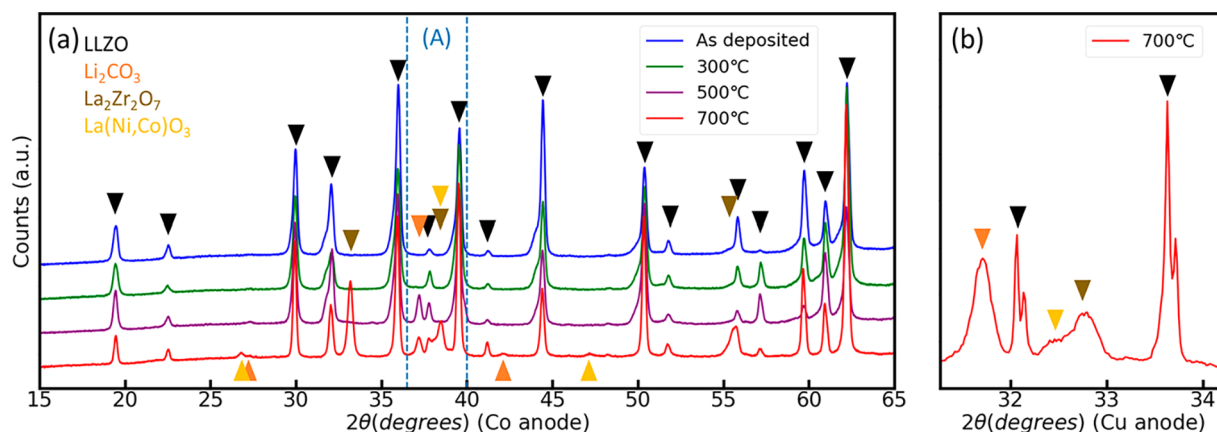


Figure 6. (a) 1D XRD pattern obtained by integration of 2D XRD patterns that were measured using the Co anode, as shown in Figures S2–S5, for the 100 nm NMC622/LLZO in the as-deposited state, and annealed at different temperatures in air. (b) 1D XRD pattern [the same region marked with dashed lines in (a)] measured using the Cu anode for the 100 nm NMC622/LLZO annealed at 700 °C in air.

The behavior at 700 °C cannot be explained by only the crystallization of the NMC film. Feature C also has a contribution from the third shell of NMC622 as shown in Figure 5c. Therefore, if NMC622 is the only phase present, feature C increase along with feature B decrease would indicate that the crystallinity of the third shell of NMC622 increases while the second shell loses crystallinity. This is contradictory to increased crystallization.

In contrast to the major changes in the Ni K-edge EXAFS, there is only a gradual increase of features A, B, and C of the Co K-edge EXAFS with increasing annealing temperature. This trend shown in Figure 5b can be explained by increased crystallization of sputtered NMC622 films, without the need of another phase to explain the data. This shows that the effect of chemical environment change around Co due to formation of La(Ni,Co)O₃ is overwhelmed by crystallization of sputtered NMC622 film. Therefore, we claim that Co does not participate as much as Ni in perovskite formation. This is consistent with our conclusion above based on the oxidation states that Ni concentration in La(Ni,Co)O₃ is higher than Co.

3.2. Structural Characterization of Secondary Phases.

XRD was done to verify the formation of La(Ni,Co)O₃ and identify other secondary phases that formed due to annealing. In Figures S2–S5, we show 2D XRD images obtained using Bruker GADDS. The intensities of each Debye ring were integrated to give 1D plots as shown in Figure 6a.

Discontinuous Debye rings are present for all samples (Figures S2–S5), and these originate from bulk LLZO grains (ICDD: 00-063-0174). The as-deposited sample (Figure S2) and the sample annealed at 300 °C (Figure S3) did not show Debye rings for secondary phases. In contrast, samples annealed at 500 °C (Figure S4) and 700 °C (Figure S5) show arcs for Li₂CO₃ (ICDD: 00-022-1141) in addition to LLZO. For the sample annealed at 700 °C (Figure S5), we also identified arcs for La₂Zr₂O₇ (ICDD: 01-070-5602). Arcs for (222) plane (33.3° [Co anode]) and (400) plane (38.7° [Co anode]) were clearly seen. In addition, we could differentiate the Debye ring for the La₂Zr₂O₇ (440) plane (55.9° [Co anode]) with the nearby LLZO because it forms a continuous ring unlike LLZO.

We also expected Debye rings corresponding to La(Ni,Co)O₃ from the sample annealed at 700 °C considering the XANES and EXAFS results. We observed peaks at 27.0 and 47.4° corresponding to the (012) and (202) planes of

LaNi_{0.5}Co_{0.5}O₃ reference spectra (ICDD: 00-054-0834), respectively. In order to give further proofs for the perovskite phase formation, we used PANalytical X'Pert Pro for a detailed scan. The result is shown in Figure 6b. Detailed scan was done within the angle range (A) shown in Figures 6a and S5 for the sample annealed at 700 °C. The angle range was chosen so that it includes the highest intensity peak for the perovskite phase. In Figure 6b, the LLZO peaks show sharp doublets because of Cu Kα₁ and Cu Kα₂ radiation. Li₂CO₃ (002) (31.8° [Cu anode]) and La₂Zr₂O₇ (400) (33.2° [Cu anode]) are clearly identifiable. In addition, an additional small peak is present just before the La₂Zr₂O₇ (400) peak. This peak could not be resolved using Bruker GADDS because of its limited resolution. This peak fits with the (110) plane of LaNi_{0.5}Co_{0.5}O₃ reference spectra (ICDD: 00-054-0834) (32.75° [Cu anode]), which is the strongest peak of the perovskite structure. This provides clear evidence for the formation of La(Ni,Co)O₃. The crystallite size of La(Ni,Co)O₃ was calculated using full width at half-maximum of XRD peak corresponding to the (110) plane using the Scherrer equation.⁴⁸ The crystallite size of La(Ni,Co)O₃ was found to be 27 nm. However, this value does not necessarily correspond to the reaction layer thickness, as the reaction layer can consist of more than one crystal size of depth.

EXAFS data (Figure 5) shows the increase of short-range order in the NMC622 film after annealing. The intensity of the features corresponding to both the Ni–O bond (1st shell) (Figure 5a) and Co–O bond (first shell) (Figure 5b) increased as annealing temperature increased. However, XRD peaks corresponding to the NMC phase could not be detected by using the Bragg–Brentano geometry. We attribute this to the reaction between NMC622 and LLZO, leading to only a small amount of NMC622 left in the system. Because of this, XRD with Bragg–Brentano geometry was not sensitive enough to the NMC phase, even when EXAFS analysis showed increase of short-range order in NMC. Signal from the bulk LLZO pellet and from the formed secondary phases overwhelmed the signals from the remaining NMC622 in the system. In order to confirm the increased crystallinity of NMC, we performed grazing incidence XRD using Rigaku SmartLab. Figure S6 shows grazing incidence XRD data for the sample annealed at 700 °C in air. A broad peak at 18.6° [Cu anode] corresponds to the XRD peak from the (003) plane of NMC622 (ICDD: 00-066-0854). Formation of a broad peak for the (003) plane

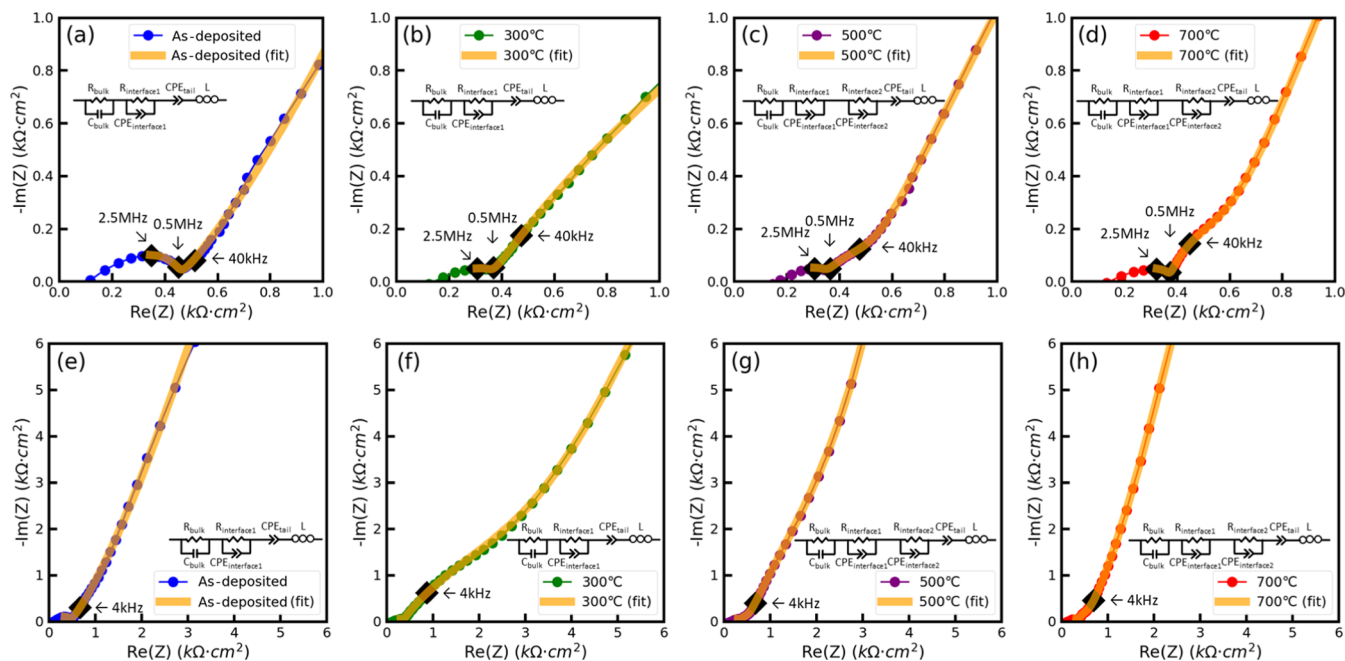


Figure 7. EIS data for AulNMC622|LLZO|NMC622|Au symmetric cells. (a–d) EIS data for frequency range where the impedance is less than 1.0 $\text{k}\Omega\text{cm}^2$ are plotted. Data for (a) as-deposited sample (7.94 MHz to 794 Hz) and samples annealed at (b) 300 °C (6.31 MHz to 3.16 kHz), (c) 500 °C (6.31 MHz to 1.26 kHz), and (d) 700 °C (6.31 MHz to 1.58 kHz) in air for 4 h are shown. (e–h) EIS data for the frequency range where the impedance is less than 6.0 $\text{k}\Omega\text{cm}^2$ are plotted. Data for (e) as-deposited sample (7.94 MHz to 63.1 Hz) and samples annealed at (f) 300 °C (6.31 MHz to 39.8 Hz), (g) 500 °C (6.31 MHz to 100 Hz), and (h) 700 °C (6.31 MHz to 158 Hz) in air for 4 h are shown.

has also been reported by previous works on RF-deposited LiCoO_2 films.^{49,50} In addition, the peak strength for the (003) plane increased as the incident angle decreased from 2 to 1°. This further justifies that the peak originated from NMC622, which had crystallized on top of the LLZO pellet. We could also observe a peak which could potentially come from the (104) plane of NMC622 (44.4° [Cu anode]). However, peak assignment was difficult to confirm because of a nearby peak from the LLZO (620) plane (44.0° [Cu anode]).

3.3. Effect of Degradation on Interfacial Resistance.

EIS allowed to quantify the impact of the interfacial chemical degradation on the electrochemical charge-transfer properties. The samples were AulNMC622|LLZO|NMC622|Au symmetric cells, with 60 nm thick NMC622 thin-film layers on both sides of polished LLZO pellets. Au was deposited as a current collector after samples were prepared and annealed in air.

Figure 7 shows the EIS data for samples with different annealing conditions. In Figure 7a–d, EIS data are shown in a narrower frequency range compared to Figure 7e–h, so that the small arcs at higher frequencies are discernible.

We used two different equivalent circuit models to analyze the EIS data. For the as-deposited sample and the sample annealed at 300 °C, we used $(R_{\text{bulk}}C_{\text{bulk}})(R_{\text{interface1}}CPE_{\text{interface1}})(CPE_{\text{tail}})(L)$ circuit because there were two semicircles. On the other hand, we used $(R_{\text{bulk}}C_{\text{bulk}})(R_{\text{interface1}}CPE_{\text{interface1}})(R_{\text{interface2}}CPE_{\text{interface2}})(CPE_{\text{tail}})(L)$ circuit for samples annealed at 500 and 700 °C as there were three apparent semicircles in the plot. Serially connected inductor comes from the wiring of the setting. This element has been used by works using LLZO pellets and improved fitting the data at the high-frequency range.^{51,52} The serially connected constant phase element corresponds to the low-frequency tail shown in Figure 7.

We observed the high-frequency semicircle ($R_{\text{bulk}}C_{\text{bulk}}$) around 2.5 MHz in all samples. This comes from the geometry

of the LLZO pellet. The conductivity and relative permittivity deduced from this arc are 2.7×10^{-1} mS/cm and ~ 80 , respectively, consistent with values reported in former works on LLZO.^{52,53}

We also identified additional arcs at 4 kHz ($R_{\text{interface1}}CPE_{\text{interface1}}$) in all samples as can be seen in Figure 7. We attribute this feature to the NMC622|LLZO charge-transfer resistance. The feature in the similar frequency range was also attributed to the interface charge-transfer resistance in our former work on LiCoO_2 |LLZO.²¹ In addition, a new arc arises around 40 kHz ($R_{\text{interface2}}CPE_{\text{interface2}}$) for the samples annealed at 500 and 700 °C. We confirmed with XRD that the sample annealed at 500 °C had Li_2CO_3 , and the sample annealed at 700 °C had Li_2CO_3 , $\text{La}(\text{Ni},\text{Co})\text{O}_3$, and $\text{La}_2\text{Zr}_2\text{O}_7$ as secondary phases. Based on those findings, we attribute this feature around 40 kHz to the impedances arising from secondary phases.

Figure 8 shows comparison of cathode/electrolyte interfacial resistance for each sample. As we used a symmetrically

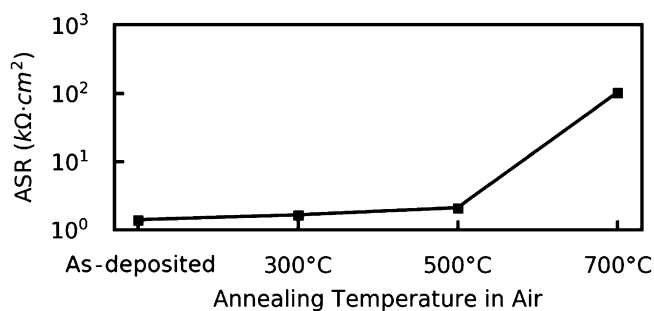


Figure 8. ASR for a single cathode/electrolyte interface from the as-deposited NMC622|LLZO and after annealing at different temperatures for 4 h in air.

constructed sample, the effect of interfacial resistance is twice as large as compared to the cell with only one cathode electrolyte interface. In order to get interfacial resistance through the single cathode electrolyte interface, Figure 8 shows the plots of $R_{\text{interface}}/2$ for cathode electrolyte interfacial resistance for the as-deposited sample and the sample annealed at 300 °C and of $(R_{\text{interface1}} + R_{\text{interface2}})/2$ for the samples annealed at 500 and 700 °C.

As can be seen in Figure 8, the area-specific resistance (ASR) increases with annealing temperature. The obtained ASR arising from the interface or from the interface reactions, for as-deposited, 300, and 500 °C treated samples are 1.4, 1.7, and 2.1, respectively. Notably, ASR increases dramatically to 102 kΩ cm² when the sample was annealed at 700 °C. This fits well with the findings from XANES, EXAFS, and XRD that major interfacial chemical and structural degradation takes place at 700 °C. Formation of phases that do not conduct Li ions, such as La₂Zr₂O₇, La(Ni,Co)O₃, and Li₂CO₃, is expected to increase the ASR at the interface.²¹

4. DISCUSSION

The first key point we discuss is that the secondary phases formed due to the interfacial degradation [La₂Zr₂O₇, La(Ni,Co)O₃, and Li₂CO₃] are not Li conductors. La₂Zr₂O₇ has poor Li conductivity, and it is a typical secondary phase found in delithiated LLZO.⁵⁴ La(Ni,Co)O₃ is not expected to be a Li conductor. There are perovskite Li conductors such as (Li,La)TiO₃, but Li conduction requires substantial A-site vacancy fraction.⁵⁵ Li₂CO₃ has much poorer Li conductivity (~10⁻³ mS/cm) at room temperature compared to LLZO.⁵⁶

There is a large difference in interfacial resistances of the sample that only contains Li₂CO₃ after exposure to 500 °C and that of the sample that contains Li₂CO₃, La₂Zr₂O₇, and La(Ni,Co)O₃ after exposure to 700 °C. The interfacial resistance found from the former was 2.1 kΩ cm² and that from the latter was 102 kΩ cm². This proves that formation of interfacial products [La₂Zr₂O₇ and La(Ni,Co)O₃] beyond Li₂CO₃ led to a substantial degradation of the charge-transfer properties of the interface. This explains the stark increase of interfacial resistance for the sample annealed at 700 °C. Complete coverage of the interface with secondary phases [Li₂CO₃, La₂Zr₂O₇, and La(Ni,Co)O₃ which are poor Li conductors] led to poor Li transfer at the interface, with 2 orders of magnitude increase in the interface impedance.

The second key point is that Ni has higher tendency than Co to participate in the formation of La(Ni,Co)O₃, as deduced from the Ni K-edge and Co K-edge EXAFS data taken from the sample annealed at 700 °C. The features for La(Ni,Co)O₃ in the Ni K-edge EXAFS spectra indicate that a substantial amount of Ni experienced a chemical environment change. In contrast, the Co K-edge EXAFS spectra could be fully explained by crystallization of the NMC film. Therefore, only a small portion of Co in the NMC622 film participated in perovskite formation and majority of those remained in NMC622.

Different reaction tendencies of transition metal cations can originate in part from their mobility in NMC lattice. With this, we mean two processes: (i) move of the transition metal to the Li sites and (ii) the migration of the transition metal once it resides at the Li sublattice. Migration of transition metal cations to the nearby octahedral site of the Li sublattice makes them mobile in the oxide.⁵⁷ Ni is able to move to the Li sites more readily than Co and Mn in NMC because the energy

needed for Li⁺/Ni²⁺ exchange is lower than that for Li⁺/Co³⁺ or Li⁺/Mn⁴⁺ exchange. The calculated formation energies for the Ni_{Li}-Li_{Ni}, Co_{Li}-Li_{Co}, and Mn_{Li}-Li_{Mn} antisite pairs in LiNi_{1/3}Co_{1/3}Mn_{1/3}O₂ are 0.57, 1.42, and 2.60 eV, respectively.⁵⁸ Moreover, Ni has a low migration barrier, ~0.25 eV, once it migrates into the Li site by Li⁺/Ni²⁺ exchange.⁵⁹ This value is on the same order of migration barrier of Li in layered oxide cathodes.⁵⁹⁻⁶² Solid-state reaction between two phases in contact requires flux of elements toward the interface. As Ni is the most mobile transition metal species in the NMC lattice, Ni flux will be larger than Co and Mn. For this reason, if there is an external chemical driver for reaction, we expect that Ni will more readily migrate to the interface and participate in the reaction.

The result suggests that increasing Ni content in the layered oxide to obtain a high power and high capacity cell can lead to inferior interfacial instability. Ni-rich cathode is already well known to react with organic electrolyte and form SEI.⁶³ Our work is the first experimental demonstration that the same problem exists in this all solid system, too.

EXAFS analysis for Mn coordination was not possible because of the overlap of La L₁ edge and Mn K edge, but XRD and oxidation state analysis indicated no detectable reactivity of Mn in our system. There were no Mn-containing secondary phases detected using XRD. The oxidation state of Mn did not change after annealing as seen by Mn L-edge spectra (Figure S1). Therefore, we conclude that Mn is not participating in the secondary-phase formation between LLZO and NMC622 in our experimental conditions.

The third key point we discuss here is the inconsistency between prior computational predictions of NMC/LLZO interfacial reactions and our experimental findings. We propose that this is because of not having considered the elevated temperature and gas environment effects. Xiao et al. predicted Li₅CoO₄, NiO, La₂O₃, Li₆Zr₂O₇, and Li₂MnO₃ formation for reaction between NMC and LLZO.¹³ Richards et al. predicted La₂Zr₂O₇, Li₂NiO₃, and La₂O₃ for LiNiO₂/LLZO and La₂Zr₂O₇, Li₂MnO₃, and La₂O₃ for LiMnO₂/LLZO.¹⁹ Both works do not predict formation of La(Ni,Co)O₃ phase, and we did not find evidence to La₂O₃ or to Li-rich transition metal oxides. Most importantly, the pervasive Li₂CO₃ formation in our experimental findings is missing from previous theoretical reports. The discrepancy between our experimental results and prior calculations could arise from two key factors. First, the computational predictions we see in the literature^{13,19} have not considered the potential role of gaseous species in the environment, in particular CO₂ and H₂O(g). We find substantial Li₂CO₃ formation as a sink of Li, consumed by CO₂. As a result, this process is not permitting the formation of the predicted lithium-rich phases such as Li₅CoO₄, Li₂NiO₃, and Li₂MnO₃. Li₂CO₃ is also responsible for the formation of delithiated phases. These are La₂Zr₂O₇ that precipitate from LLZO and La(Ni,Co)O₃ that can form as a reaction product when LLZO and NMC are delithiated and become more unstable. As neither NMC622 nor LLZO contains carbon, the reaction requires substantial carbon influx from outside the sample to proceed. Because we annealed the sample in air, CO₂ is the carbon source. This shows the importance of the gas environment in the interfacial degradation. Based on this, we argue that controlling the gas environment, especially P_{CO₂}, during the synthesis of these interfaces is important in achieving better stability.

Another reason behind the seeming discrepancy is likely the effect of entropy, which becomes important at higher temperatures. Both Xiao et al. and Richards et al. calculated energies for phases which are in ground state or in equilibrium at a certain composition and used those to find the reaction giving largest driving force.^{13,19} However, as Xiao et al. noted in their work, this approach could underestimate the effect of configurational entropy at elevated temperatures.⁶⁴

The results presented in this paper prompt us to hypothesize that CO₂ is the major contributor for interfacial degradation between NMC622 and LLZO at elevated temperature. Li₂CO₃ forms by reacting with CO₂ in ambient air. This reaction reduces the Li content in NMC and in LLZO, rendering them less stable. As a result, delithiated phases, La(Ni,Co)O₃ and La₂Zr₂O₇, form between NMC and LLZO. This hypothesis warrants more work to probe the NMC/LLZO interface after subjecting it to different gas conditions, and that is the topic of an upcoming paper of us.

5. CONCLUSIONS

In this work, we revealed products of interfacial reactions at NMC622/LLZO during annealing, starting with onset temperatures as low as 500 °C in air. This was possible by using thin-film cathodes within the detection depth of near-surface-sensitive techniques and by combining findings from synchrotron-based XANES and EXAFS with lab-based XRD. Major decomposition products, Li₂CO₃, La₂Zr₂O₇, and La(Ni,Co)O₃, were found in the sample annealed at 700 °C. In contrast, such phases were not present in the sample annealed at 300 °C, and only Li₂CO₃ was present in the sample annealed at 500 °C. Identification of La(Ni,Co)O₃, with substantial Ni content, was possible by careful analysis of XANES and EXAFS data. Ni was found to be more reactive than Co in forming this secondary phase at the LLZO interface. Importantly, the formed secondary phases are detrimental to the electrochemical properties. ASR at the cathode/electrolyte interface increased by 2 orders of magnitude after annealing up to 700 °C compared to the as-prepared NMC622/LLZO. Based on these results, we can conclude that using low-temperature processing is necessary to avoid detrimental secondary-phase formation if the production is done in air. Considering the reactants and products of the degrading reaction, we hypothesize that CO₂ is the major contributor for interfacial degradation between NMC622 and LLZO at elevated temperature, and we suggest using a gas environment that do not contain CO₂ to minimize interfacial degradation.

■ ASSOCIATED CONTENT

SI Supporting Information

The Supporting Information is available free of charge at <https://pubs.acs.org/doi/10.1021/acs.chemmater.0c02261>.

Experimental details, Mn L-edge XANES data, 2D XRD patterns, and grazing incidence XRD patterns (PDF)

■ AUTHOR INFORMATION

Corresponding Author

Bilge Yildiz – *Laboratory for Electrochemical Interfaces, Department of Nuclear Science and Engineering and Department of Materials Science and Engineering, Massachusetts Institute of Technology, Cambridge,*

Massachusetts 02139, United States; orcid.org/0000-0002-2688-5666; Email: byildiz@mit.edu

Authors

Younggyu Kim – *Laboratory for Electrochemical Interfaces, Department of Materials Science and Engineering, Massachusetts Institute of Technology, Cambridge, Massachusetts 02139, United States;* orcid.org/0000-0002-8489-8457

Dongha Kim – *Laboratory for Electrochemical Interfaces, Department of Materials Science and Engineering, Massachusetts Institute of Technology, Cambridge, Massachusetts 02139, United States;* orcid.org/0000-0002-8072-9808

Roland Bliem – *Laboratory for Electrochemical Interfaces, Department of Nuclear Science and Engineering, Massachusetts Institute of Technology, Cambridge, Massachusetts 02139, United States;* orcid.org/0000-0002-8714-8942

Gülin Vardar – *Laboratory for Electrochemical Interfaces, Department of Nuclear Science and Engineering, Massachusetts Institute of Technology, Cambridge, Massachusetts 02139, United States;* orcid.org/0000-0001-5458-9568

Iradwikanari Waluyo – *National Synchrotron Light Source II, Brookhaven National Laboratory, Upton, New York 11973, United States;* orcid.org/0000-0002-4046-9722

Adrian Hunt – *National Synchrotron Light Source II, Brookhaven National Laboratory, Upton, New York 11973, United States*

Joshua T. Wright – *Advanced Photon Source, Argonne National Laboratory, Lemont, Illinois 60439, United States*

John P. Katsoudas – *Advanced Photon Source, Argonne National Laboratory, Lemont, Illinois 60439, United States*

Complete contact information is available at:

<https://pubs.acs.org/10.1021/acs.chemmater.0c02261>

Notes

The authors declare no competing financial interest.

■ ACKNOWLEDGMENTS

This research has been funded by U.S. Army Research Office through Institute for Soldier Nanotechnologies (Cooperative Agreement Number W911NF-18-2-0048). This work made use of the Shared Experimental Facilities supported in part by the MRSEC Program of the National Science Foundation under award number DMR1419807. XANES data were acquired at 23-ID-2(10S) of the National Synchrotron Light Source II, a U.S. Department of Energy (DOE) Office of Science User Facility, which is operated for the DOE Office of Science by Brookhaven National Laboratory (contract no. DE-SC0012704). EXAFS data were obtained at 10-ID-B of the Advanced Photon Source, a U.S. Department of Energy (DOE) Office of Science User Facility, which is operated for the DOE Office of Science by Argonne National Laboratory (contract no. DE-AC02-06CH11357). We thank Yet-Ming Chiang and Ju Li for helpful discussions. We thank Ji-Won Jung, Seungchan Ryu, and Md Anisur Rahman for their help during data acquisition at synchrotron experiments and Dino Klotz, Sang-Joon Kim, and Xiahui Yao for their help with EIS measurements.

REFERENCES

- (1) Hess, S.; Wohlfahrt-Mehrens, M.; Wachtler, M. Flammability of Li-Ion Battery Electrolytes: Flash Point and Self-Extinguishing Time Measurements. *J. Electrochem. Soc.* **2015**, *162*, A3084–A3097.
- (2) Takada, K. Progress and Prospective of Solid-State Lithium Batteries. *Acta Mater.* **2013**, *61*, 759–770.
- (3) Manthiram, A.; Yu, X.; Wang, S. Lithium Battery Chemistries Enabled by Solid-State Electrolytes. *Nat. Rev. Mater.* **2017**, *2*, 16103.
- (4) Liu, Q.; Geng, Z.; Han, C.; Fu, Y.; Li, S.; He, Y.-b.; Kang, F.; Li, B. Challenges and Perspectives of Garnet Solid Electrolytes for All Solid-State Lithium Batteries. *J. Power Sources* **2018**, *389*, 120–134.
- (5) Thompson, T.; Yu, S.; Williams, L.; Schmidt, R. D.; Garcia-Mendez, R.; Wolfenstine, J.; Allen, J. L.; Kioupakis, E.; Siegel, D. J.; Sakamoto, J. Electrochemical Window of the Li-Ion Solid Electrolyte $\text{Li}_7\text{La}_3\text{Zr}_2\text{O}_{12}$. *ACS Energy Lett.* **2017**, *2*, 462–468.
- (6) Tarascon, J.-M.; Armand, M. Issues and Challenges Facing Rechargeable Lithium Batteries. *Nature* **2001**, *414*, 359–367.
- (7) Ren, Y.; Shen, Y.; Lin, Y.; Nan, C.-W. Direct Observation of Lithium Dendrites inside Garnet-Type Lithium-Ion Solid Electrolyte. *Electrochem. Commun.* **2015**, *57*, 27–30.
- (8) Cheng, E. J.; Sharafi, A.; Sakamoto, J. Intergranular Li Metal Propagation through Polycrystalline $\text{Li}_{6.25}\text{Al}_{0.25}\text{La}_3\text{Zr}_2\text{O}_{12}$ Ceramic Electrolyte. *Electrochim. Acta* **2017**, *223*, 85–91.
- (9) Tsai, C.-L.; Roddatis, V.; Chandran, C. V.; Ma, Q.; Uhlenbruck, S.; Bram, M.; Heitjans, P.; Guillon, O. $\text{Li}_7\text{La}_3\text{Zr}_2\text{O}_{12}$ Interface Modification for Li Dendrite Prevention. *ACS Appl. Mater. Interfaces* **2016**, *8*, 10617–10626.
- (10) Duan, H.; Yin, Y.-X.; Shi, Y.; Wang, P.-F.; Zhang, X.-D.; Yang, C.-P.; Shi, J.-L.; Wen, R.; Guo, Y.-G.; Wan, L.-J. Dendrite-Free Li-Metal Battery Enabled by a Thin Asymmetric Solid Electrolyte with Engineered Layers. *J. Am. Chem. Soc.* **2018**, *140*, 82–85.
- (11) Wu, B.; Wang, S.; Lochala, J.; Desrochers, D.; Liu, B.; Zhang, W.; Yang, J.; Xiao, J. The Role of the Solid Electrolyte Interphase Layer in Preventing Li Dendrite Growth in Solid-State Batteries. *Energy Environ. Sci.* **2018**, *11*, 1803–1810.
- (12) Han, X.; Gong, Y.; Fu, K.; He, X.; Hitz, G. T.; Dai, J.; Pearse, A.; Liu, B.; Wang, H.; Rubloff, G.; Mo, Y.; Thangadurai, V.; Wachsmann, E. D.; Hu, L. Negating Interfacial Impedance in Garnet-Based Solid-State Li Metal Batteries. *Nat. Mater.* **2017**, *16*, 572.
- (13) Xiao, Y.; Miara, L. J.; Wang, Y.; Ceder, G. Computational Screening of Cathode Coatings for Solid-State Batteries. *Joule* **2019**, *3*, 1252–1275.
- (14) Zhu, Y.; He, X.; Mo, Y. First Principles Study on Electrochemical and Chemical Stability of Solid Electrolyte–Electrode Interfaces in All-Solid-State Li-Ion Batteries. *J. Mater. Chem. A* **2016**, *4*, 3253–3266.
- (15) Park, K.; Yu, B.-C.; Jung, J.-W.; Li, Y.; Zhou, W.; Gao, H.; Son, S.; Goodenough, J. B. Electrochemical Nature of the Cathode Interface for a Solid-State Lithium-Ion Battery: Interface between LiCoO_2 and Garnet- $\text{Li}_7\text{La}_3\text{Zr}_2\text{O}_{12}$. *Chem. Mater.* **2016**, *28*, 8051–8059.
- (16) Ren, Y.; Liu, T.; Shen, Y.; Lin, Y.; Nan, C.-W. Chemical Compatibility between Garnet-like Solid State Electrolyte $\text{Li}_{6.75}\text{La}_3\text{Zr}_{1.75}\text{Ta}_{0.25}\text{O}_{12}$ and Major Commercial Lithium Battery Cathode Materials. *J. Materiomics* **2016**, *2*, 256–264.
- (17) Kim, K. H.; Iriyama, Y.; Yamamoto, K.; Kumazaki, S.; Asaka, T.; Tanabe, K.; Fisher, C. A. J.; Hirayama, T.; Murugan, R.; Ogumi, Z. Characterization of the Interface between LiCoO_2 and $\text{Li}_7\text{La}_3\text{Zr}_2\text{O}_{12}$ in an All-Solid-State Rechargeable Lithium Battery. *J. Power Sources* **2011**, *196*, 764–767.
- (18) Uhlenbruck, S.; Dornseiffer, J.; Lobe, S.; Dellen, C.; Tsai, C.-L.; Gotzen, B.; Sebold, D.; Finsterbusch, M.; Guillon, O. Cathode-Electrolyte Material Interactions during Manufacturing of Inorganic Solid-State Lithium Batteries. *J. Electroceram.* **2017**, *38*, 197–206.
- (19) Richards, W. D.; Miara, L. J.; Wang, Y.; Kim, J. C.; Ceder, G. Interface Stability in Solid-State Batteries. *Chem. Mater.* **2016**, *28*, 266–273.
- (20) Zhang, N.; Long, X.; Wang, Z.; Yu, P.; Han, F.; Fu, J.; Ren, G.; Wu, Y.; Zheng, S.; Huang, W.; Wang, C.; Li, H.; Liu, X. Mechanism Study on the Interfacial Stability of a Lithium Garnet-Type Oxide Electrolyte against Cathode Materials. *ACS Appl. Energy Mater.* **2018**, *1*, 5968–5976.
- (21) Vardar, G.; Bowman, W. J.; Lu, Q.; Wang, J.; Chater, R. J.; Aguadero, A.; Seibert, R.; Terry, J.; Hunt, A.; Waluyo, I.; Fong, D. D.; Jarry, A.; Crumlin, E. J.; Hellstrom, S. L.; Chiang, Y.-M.; Yildiz, B. Structure, Chemistry, and Charge Transfer Resistance of the Interface between $\text{Li}_7\text{La}_3\text{Zr}_2\text{O}_{12}$ Electrolyte and LiCoO_2 Cathode. *Chem. Mater.* **2018**, *30*, 6259–6276.
- (22) Chebiam, R. V.; Kannan, A. M.; Prado, F.; Manthiram, A. Comparison of the Chemical Stability of the High Energy Density Cathodes of Lithium-Ion Batteries. *Electrochem. Commun.* **2001**, *3*, 624–627.
- (23) Zheng, J.; Liu, T.; Hu, Z.; Wei, Y.; Song, X.; Ren, Y.; Wang, W.; Rao, M.; Lin, Y.; Chen, Z.; Lu, J.; Wang, C.; Amine, K.; Pan, F. Tuning of Thermal Stability in Layered $\text{Li}(\text{Ni}_x\text{Mn}_y\text{Co}_z)\text{O}_2$. *J. Am. Chem. Soc.* **2016**, *138*, 13326–13334.
- (24) Li, W.; Song, B.; Manthiram, A. High-Voltage Positive Electrode Materials for Lithium-Ion Batteries. *Chem. Soc. Rev.* **2017**, *46*, 3006–3059.
- (25) Stöhr, J. *NEXAFS Spectroscopy*; Springer: Berlin; London, 2011.
- (26) Wang, B.; Bates, J. B.; Hart, F. X.; Sales, B. C.; Zuh, R. A.; Robertson, J. D. Characterization of Thin-Film Rechargeable Lithium Batteries with Lithium Cobalt Oxide Cathodes. *J. Electrochem. Soc.* **1996**, *143*, 3203.
- (27) Zhu, X.; Guo, Z.; Du, G.; Zhang, P.; Liu, H. LiCoO_2 Cathode Thin Film Fabricated by RF Sputtering for Lithium Ion Micro-batteries. *Surf. Coat. Technol.* **2010**, *204*, 1710–1714.
- (28) Kim, H.-S.; Oh, Y.; Kang, K. H.; Kim, J. H.; Kim, J.; Yoon, C. S. Characterization of Sputter-Deposited LiCoO_2 Thin Film Grown on NASICON-Type Electrolyte for Application in All-Solid-State Rechargeable Lithium Battery. *ACS Appl. Mater. Interfaces* **2017**, *9*, 16063–16070.
- (29) Bates, J. B.; Dudney, N. J.; Neudecker, B. J.; Hart, F. X.; Jun, H. P.; Hackney, S. A. Preferred Orientation of Polycrystalline LiCoO_2 Films. *J. Electrochem. Soc.* **2000**, *147*, 59–70.
- (30) de Groot, F. M. F.; Grioni, M.; Fuggle, J. C.; Ghijssen, J.; Sawatzky, G. A.; Petersen, H. Oxygen 1s x-Ray-Absorption Edges of Transition-Metal Oxides. *Phys. Rev. B: Condens. Matter Mater. Phys.* **1989**, *40*, 5715–5723.
- (31) Suntiwich, J.; Hong, W. T.; Lee, Y.-L.; Rondinelli, J. M.; Yang, W.; Goodenough, J. B.; Dabrowski, B.; Freeland, J. W.; Shao-Horn, Y. Estimating Hybridization of Transition Metal and Oxygen States in Perovskites from O K -Edge X-Ray Absorption Spectroscopy. *J. Phys. Chem. C* **2014**, *118*, 1856–1863.
- (32) Cheng, L.; Crumlin, E. J.; Chen, W.; Qiao, R.; Hou, H.; Franz Lux, S.; Zorba, V.; Russo, R.; Kosteki, R.; Liu, Z.; Persson, K.; Yang, W.; Cabana, J.; Richardson, T.; Chen, G.; Doeff, M. The Origin of High Electrolyte–Electrode Interfacial Resistances in Lithium Cells Containing Garnet Type Solid Electrolytes. *Phys. Chem. Chem. Phys.* **2014**, *16*, 18294–18300.
- (33) Hwang, S.; Kim, S. M.; Bak, S.-M.; Kim, S. Y.; Cho, B.-W.; Chung, K. Y.; Lee, J. Y.; Stach, E. A.; Chang, W. Using Real-Time Electron Microscopy To Explore the Effects of Transition-Metal Composition on the Local Thermal Stability in Charged $\text{Li}_x\text{Ni}_y\text{Mn}_z\text{Co}_{1-y-z}\text{O}_2$ Cathode Materials. *Chem. Mater.* **2015**, *27*, 3927–3935.
- (34) Tian, C.; Nordlund, D.; Xin, H. L.; Xu, Y.; Liu, Y.; Sokaras, D.; Lin, F.; Doeff, M. M. Depth-Dependent Redox Behavior of $\text{LiNi}_{0.6}\text{Mn}_{0.2}\text{Co}_{0.2}\text{O}_2$. *J. Electrochem. Soc.* **2018**, *165*, A696–A704.
- (35) Lin, F.; Markus, I. M.; Nordlund, D.; Weng, T.-C.; Asta, M. D.; Xin, H. L.; Doeff, M. M. Surface Reconstruction and Chemical Evolution of Stoichiometric Layered Cathode Materials for Lithium-Ion Batteries. *Nat. Commun.* **2014**, *5*, 3529.
- (36) Xu, J.; Hu, E.; Nordlund, D.; Mehta, A.; Ehrlich, S. N.; Yang, X.-Q.; Tong, W. Understanding the Degradation Mechanism of Lithium Nickel Oxide Cathodes for Li-Ion Batteries. *ACS Appl. Mater. Interfaces* **2016**, *8*, 31677–31683.

- (37) Merz, M.; Nagel, P.; Pinta, C.; Samartsev, A.; Löhneysen, H. v.; Wissinger, M.; Uebe, S.; Assmann, A.; Fuchs, D.; Schuppler, S. X-Ray Absorption and Magnetic Circular Dichroism of LaCoO_3 , $\text{La}_{0.7}\text{Ce}_{0.3}\text{CoO}_3$, and $\text{La}_{0.7}\text{Sr}_{0.3}\text{CoO}_3$ Films: Evidence for Cobalt-Valence-Dependent Magnetism. *Phys. Rev. B: Condens. Matter Mater. Phys.* **2010**, *82*, 174416.
- (38) Huang, M.-J. The Electronic Structure and Magnetic Interactions in the Mixed Transition-Metal Oxide $\text{La}(\text{Co,Ni})\text{O}_3$ Studied by X-Ray Absorption Spectroscopies. Doctor of Science, Karlsruhe Institut für Technologie, 2016.
- (39) Pérez, J.; García, J.; Blasco, J.; Stankiewicz, J. Spin-Glass Behavior and Giant Magnetoresistance in the (RE) $\text{Ni}_{0.3}\text{Co}_{0.7}\text{O}_3$ (RE = La, Nd, Sm) System. *Phys. Rev. Lett.* **1998**, *80*, 2401–2404.
- (40) Miyoshi, S.; Yamaguchi, S. Soft X-Ray Absorption and Photoemission Study on the Electronic Structure of $(\text{La,Sr})\text{CoO}_3$. *ECS Trans.* **2015**, *68*, 591–597.
- (41) Karvonen, L.; Valkeapää, M.; Liu, R.-S.; Chen, J.-M.; Yamauchi, H.; Karppinen, M. O-K and Co-L XANES Study on Oxygen Intercalation in Perovskite $\text{SrCoO}_{3-\delta}$. *Chem. Mater.* **2010**, *22*, 70–76.
- (42) Henderson, G. S.; de Groot, F. M. F.; Moulton, B. J. A. X-Ray Absorption Near-Edge Structure (XANES) Spectroscopy. *Rev. Mineral. Geochem.* **2014**, *78*, 75–138.
- (43) Gilbert, B.; Frazer, B. H.; Belz, A.; Conrad, P. G.; Neelson, K. H.; Haskel, D.; Lang, J. C.; Srajer, G.; De Stasio, G. Multiple Scattering Calculations of Bonding and X-Ray Absorption Spectroscopy of Manganese Oxides. *J. Phys. Chem. A* **2003**, *107*, 2839–2847.
- (44) Bak, S.-M.; Nam, K.-W.; Chang, W.; Yu, X.; Hu, E.; Hwang, S.; Stach, E. A.; Kim, K.-B.; Chung, K. Y.; Yang, X.-Q. Correlating Structural Changes and Gas Evolution during the Thermal Decomposition of Charged $\text{Li}_x\text{Ni}_{0.8}\text{Co}_{0.15}\text{Al}_{0.05}\text{O}_2$ Cathode Materials. *Chem. Mater.* **2013**, *25*, 337–351.
- (45) Aryal, S.; Timofeeva, E. V.; Segre, C. U. Structural Studies of Capacity Activation and Reduced Voltage Fading in Li-Rich, Mn-Ni-Fe Composite Oxide Cathode. *J. Electrochem. Soc.* **2018**, *165*, A71–A78.
- (46) Deb, A.; Bergmann, U.; Cramer, S. P.; Cairns, E. J. In Situ x-Ray Absorption Spectroscopic Study of the $\text{Li}[\text{Ni}_{1/3}\text{Co}_{1/3}\text{Mn}_{1/3}]\text{O}_2$ Cathode Material. *J. Appl. Phys.* **2005**, *97*, 113523.
- (47) Jain, A.; Ong, S. P.; Hautier, G.; Chen, W.; Richards, W. D.; Dacek, S.; Cholia, S.; Gunter, D.; Skinner, D.; Ceder, G.; Persson, K. A. Commentary: The Materials Project: A Materials Genome Approach to Accelerating Materials Innovation. *APL Mater.* **2013**, *1*, 011002.
- (48) Langford, J. I.; Wilson, A. J. C. Scherrer after Sixty Years: A Survey and Some New Results in the Determination of Crystallite Size. *J. Appl. Crystallogr.* **1978**, *11*, 102–113.
- (49) Bouwman, P. J.; Boukamp, B. A.; Bouwmeester, H. J. M.; Wondergem, H. J.; Notten, P. H. L. Structural Analysis of Submicrometer LiCoO_2 Films. *J. Electrochem. Soc.* **2001**, *148*, A311–A317.
- (50) Jeon, S.-W.; Lim, J.-K.; Lim, S.-H.; Lee, S.-M. As-Deposited LiCoO_2 Thin Film Cathodes Prepared by Rf Magnetron Sputtering. *Electrochim. Acta* **2005**, *51*, 268–273.
- (51) Rettenwander, D.; Welzl, A.; Cheng, L.; Fleig, J.; Musso, M.; Suard, E.; Doeff, M. M.; Redhammer, G. J.; Amthauer, G. Synthesis Crystal Chemistry, and Electrochemical Properties of $\text{Li}_{7-2x}\text{La}_3\text{Zr}_{2-x}\text{Mo}_x\text{O}_{12}$ ($x = 0.1-0.4$): Stabilization of the Cubic Garnet Polymorph via Substitution of Zr^{4+} by Mo^{6+} . *Inorg. Chem.* **2015**, *54*, 10440–10449.
- (52) Wachter-Welzl, A.; Kirowitz, J.; Wagner, R.; Smetacek, S.; Brunauer, G. C.; Bonta, M.; Rettenwander, D.; Taibl, S.; Limbeck, A.; Amthauer, G.; Fleig, J. The Origin of Conductivity Variations in Al-Stabilized $\text{Li}_7\text{La}_3\text{Zr}_2\text{O}_{12}$ Ceramics. *Solid State Ionics* **2018**, *319*, 203–208.
- (53) Wachter-Welzl, A.; Wagner, R.; Rettenwander, D.; Taibl, S.; Amthauer, G.; Fleig, J. Microelectrodes for Local Conductivity and Degradation Measurements on Al Stabilized $\text{Li}_7\text{La}_3\text{Zr}_2\text{O}_{12}$ Garnets. *J. Electroceram.* **2017**, *38*, 176–181.
- (54) Chen, Y.; Rangasamy, E.; dela Cruz, C. R.; Liang, C.; An, K. A Study of Suppressed Formation of Low-Conductivity Phases in Doped $\text{Li}_7\text{La}_3\text{Zr}_2\text{O}_{12}$ Garnets by in Situ Neutron Diffraction. *J. Mater. Chem. A* **2015**, *3*, 22868–22876.
- (55) Alonso, J. A.; Sanz, J.; Santamaría, J.; León, C.; Várez, A.; Fernández-Díaz, M. T. On the Location of Li^+ Cations in the Fast Li-Cation Conductor $\text{La}_{0.5}\text{Li}_{0.5}\text{TiO}_3$ Perovskite. *Angew. Chem., Int. Ed.* **2000**, *39*, 619–621.
- (56) Ebrahiminia, M.; Hooper, J.; Bedrov, D. Structural, Mechanical, and Dynamical Properties of Amorphous Li_2CO_3 from Molecular Dynamics Simulations. *Crystals* **2018**, *8*, 473.
- (57) Reed, J.; Ceder, G. Role of Electronic Structure in the Susceptibility of Metastable Transition-Metal Oxide Structures to Transformation. *Chem. Rev.* **2004**, *104*, 4513–4534.
- (58) Hoang, K.; Johannes, M. Defect Physics and Chemistry in Layered Mixed Transition Metal Oxide Cathode Materials: (Ni,Co,Mn) vs (Ni,Co,Al). *Chem. Mater.* **2016**, *28*, 1325–1334.
- (59) Gu, M.; Belharouak, I.; Genc, A.; Wang, Z.; Wang, D.; Amine, K.; Gao, F.; Zhou, G.; Thevuthasan, S.; Baer, D. R.; Zhang, J.-G.; Browning, N. D.; Liu, J.; Wang, C. Conflicting Roles of Nickel in Controlling Cathode Performance in Lithium Ion Batteries. *Nano Lett.* **2012**, *12*, 5186–5191.
- (60) Moradabadi, A.; Kaghazchi, P. Mechanism of Li Intercalation/Deintercalation into/from the Surface of LiCoO_2 . *Phys. Chem. Chem. Phys.* **2015**, *17*, 22917–22922.
- (61) Ning, F.; Li, S.; Xu, B.; Ouyang, C. Strain Tuned Li Diffusion in LiCoO_2 Material for Li Ion Batteries: A First Principles Study. *Solid State Ionics* **2014**, *263*, 46–48.
- (62) Ong, S. P.; Chevrier, V. L.; Hautier, G.; Jain, A.; Moore, C.; Kim, S.; Ma, X.; Ceder, G. Voltage, Stability and Diffusion Barrier Differences between Sodium-Ion and Lithium-Ion Intercalation Materials. *Energy Environ. Sci.* **2011**, *4*, 3680.
- (63) Manthiram, A. Electrical Energy Storage: Materials Challenges and Prospects. *MRS Bull.* **2016**, *41*, 624–631.
- (64) Xiao, Y.; Wang, Y.; Bo, S.-H.; Kim, J. C.; Miara, L. J.; Ceder, G. Understanding Interface Stability in Solid-State Batteries. *Nat. Rev. Mater.* **2020**, *5*, 105–126.